Correction

EARTH, ATMOSPHERIC, AND PLANETARY SCIENCES

Correction for "Reassessing the atmospheric oxidation mechanism of toluene," by Yuemeng Ji, Jun Zhao, Hajime Terazono, Kentaro Misawa, Nicholas P. Levitt, Yixin Li, Yun Lin, Jianfei Peng, Yuan Wang, Lian Duan, Bowen Pan, Fang Zhang, Xidan Feng, Taicheng An, Wilmarie Marrero-Ortiz, Jeremiah Secrest, Annie L. Zhang, Kazuhiko Shibuya, Mario J. Molina, and Renyi Zhang, which was first published July 17, 2017; 10.1073/pnas.1705463114 (*Proc Natl Acad Sci USA* 114:8169–8174).

The authors note that, due to a printer's error, Table 2 appeared incorrectly. The corrected table appears below.

Table 2. Summary of activation energy (E_a, kcal·mol^{-1}), reaction energy (ΔE_r, kcal·mol^{-1}), rate constant (k, cm^3·molecule^{-1}·s^{-1}), and branching ratio (Γ) of the OH–toluene reactions at 298 K

Reactions	Quantity	*Ortho*	*Para*	*Meta*
Toluene + OH → OH-adduct	E_a	1.2	2.1	2.7
	ΔE_r	−15.5	−14.6	−14.4
	k	2.7×10^{-12}	7.4×10^{-13}	1.2×10^{-13}
	Γ (%)	74, 80.6*, 52†, 59‡	21, 14.3*, 34†, 14‡	3, 5.1*, 11†, 5‡
OH-adduct + O_2 → Cresol	E_a	4.4, 3.7§	4.1	5.0
	ΔE_r	−26.3, −28.7§	−26.8	−27.0
	k	1.6×10^{-15}, 0.9×10^{-15}‡, 5.1×10^{-15}§	2.4×10^{-15}, 1.7×10^{-15}‡	1.2×10^{-16}
OH-adduct + O_2 → $RO_2^{\bullet}$	E_a	7.5, 7.1§	0.8	−0.4
	ΔE_r	−8.5, −2.9§	−12.2	−9.5
	k	1.5×10^{-16}, 2.8×10^{-16}‡, 1.0×10^{-17}§, 3×10^{-15}¶	2.5×10^{-14}, 1.5×10^{-14}‡	4.5×10^{-15}
o-Cresol + OH → DHMB	E_a	−0.4		
	ΔE_r	−15.6		
	k	4.3×10^{-11}, 4.3×10^{-11}#		
DHMD + O_2 → 1,2-dihydroxy-3-methylbenzene	E_a	2.2		
	ΔE_r	−24.3		
	k	5.4×10^{-12}		

The value is from the present work, except noted otherwise. Γ is calculated by excluding those from the OH *ipso* addition and the H-abstraction pathways.
*From ref. 30.
†From ref. 22, including a branching ratio of 3% for OH *ipso* addition.
‡From ref. 23, including a branching ratio of 15% for *ipso* position.
§From ref. 26.
¶From ref. 10.
#From ref. 41.

www.pnas.org/cgi/doi/10.1073/pnas.1715304114

Reassessing the atmospheric oxidation mechanism of toluene

Yuemeng Ji[a,b,c,1], Jun Zhao[c,d,1], Hajime Terazono[c,e], Kentaro Misawa[c,e,2], Nicholas P. Levitt[c,3], Yixin Li[f], Yun Lin[c], Jianfei Peng[c], Yuan Wang[g], Lian Duan[c,h], Bowen Pan[c], Fang Zhang[c,i], Xidan Feng[c,j], Taicheng An[a,b,4], Wilmarie Marrero-Ortiz[f], Jeremiah Secrest[f], Annie L. Zhang[k], Kazuhiko Shibuya[e], Mario J. Molina[l,4], and Renyi Zhang[c,f,4]

[a]Institute of Environmental Health and Pollution Control, Guangdong University of Technology, Guangzhou 510006, China; [b]Guangzhou Key Laboratory of Environmental Catalysis and Pollution Control, School of Environmental Science and Engineering, Guangdong University of Technology, Guangzhou 510006, China; [c]Department of Atmospheric Sciences, Texas A&M University, College Station, TX 77843; [d]Guangdong Province Key Laboratory for Climate Change and Natural Disaster Studies, Institute of Earth Climate and Environment System, School of Atmospheric Sciences, Sun Yat-sen University, Guangzhou 510275, China; [e]Department of Chemistry, Graduate School of Science and Engineering, Tokyo Institute of Technology, Tokyo 152-8551, Japan; [f]Department of Chemistry, Texas A&M University, College Station, TX 77840; [g]Division of Geological and Planetary Sciences, California Institute of Technology, Pasadena, CA 91125; [h]School of Resource and Environmental Engineering, East China University of Science and Technology, Shanghai 200237, China; [i]State Key Laboratory of Earth Surface Processes and Resource Ecology, College of Global Change and Earth System Science, Beijing Normal University, Beijing 100875, China; [j]College of Environmental Science and Engineering, Zhongkai University of Agriculture and Engineering, Guangzhou 510225, China; [k]Department of Chemistry, College of Natural Sciences, The University of Texas at Austin, Austin, TX 78712; and [l]Department of Chemistry and Biochemistry, University of California, San Diego, La Jolla, CA 92093

Contributed by Mario J. Molina, June 8, 2017 (sent for review April 3, 2017; reviewed by Sasha Madronich and Fangqun Yu)

Photochemical oxidation of aromatic hydrocarbons leads to tropospheric ozone and secondary organic aerosol (SOA) formation, with profound implications for air quality, human health, and climate. Toluene is the most abundant aromatic compound under urban environments, but its detailed chemical oxidation mechanism remains uncertain. From combined laboratory experiments and quantum chemical calculations, we show a toluene oxidation mechanism that is different from the one adopted in current atmospheric models. Our experimental work indicates a larger-than-expected branching ratio for cresols, but a negligible formation of ring-opening products (e.g., methylglyoxal). Quantum chemical calculations also demonstrate that cresols are much more stable than their corresponding peroxy radicals, and, for the most favorable OH (*ortho*) addition, the pathway of H extraction by O_2 to form the cresol proceeds with a smaller barrier than O_2 addition to form the peroxy radical. Our results reveal that phenolic (rather than peroxy radical) formation represents the dominant pathway for toluene oxidation, highlighting the necessity to reassess its role in ozone and SOA formation in the atmosphere.

aromatics | oxidation | ozone | secondary organic aerosol | air pollution

Toluene is the most abundant aromatic hydrocarbon in the atmosphere and is emitted primarily from anthropogenic sources, i.e., from automobiles and industrial activities. Photochemical oxidation of toluene plays an important role in tropospheric ozone and secondary organic aerosol (SOA) formation, profoundly impacting air quality, human health, and climate (1–8). However, the detailed chemical mechanism of toluene oxidation in the atmosphere remains uncertain (4, 5). Oxidation of toluene is initiated by the hydroxyl radical (OH): the initial OH–toluene reaction results in minor H abstraction (about 10%) and major OH addition (about 90%) (9–20). The H-abstraction pathway leads to the formation of benzaldehyde, whose oxidative pathway is well established (4, 5). The OH addition pathway results in the formation of methylhydroxycyclohexadienyl radicals (the OH–toluene adducts), which subsequently react with O_2 via three plausible pathways (Fig. 1), i.e., H abstraction to yield phenolic compounds and hydroperoxy radicals (HO_2) (pathway I), O_2 addition to form primary peroxy radicals or RO_2 (pathway II), and H abstraction and subsequent O-bridge formation to aromatic oxide/oxepin (pathway III). Previous theoretical studies have suggested that the primary RO_2 cyclizes to form bicyclic radicals, rather than reacting with NO to form alkoxy radicals under atmospheric conditions (16). The bicyclic radicals then undergo unimolecular rearrangement, followed by H abstraction, to form epoxide intermediates or react with O_2 to form secondary RO_2, followed by ring cleavage to produce small α-carbonyl compounds such as glyoxal and methylglyoxal (16, 21). The toluene–oxide/methyloxepin channel remains speculative, and several previous quantum chemical calculations have shown a high barrier for this pathway (22–26). Numerous experimental studies have been performed to investigate the products from the OH–toluene reactions (2–5, 18, 27). For example, previous studies have reported a highly variable yield of cresols (11, 12, 15, 18, 19, 27), ranging from 9.0 to 52.9%. In addition, the yields of glyoxal and methylglyoxal determined from the previous studies are also conflicting, ranging from <4% to about 39% for glyoxal and <4 to 17% for methylglyoxal (12, 13, 18). From an atmospheric modeling perspective (2–5), ozone

Significance

Aromatic hydrocarbons account for 20 to 30% of volatile organic compounds and contribute importantly to ozone and secondary organic aerosol (SOA) formation in urban environments. The oxidation of toluene, the most abundant aromatic compound, is believed to occur mainly via OH addition, primary organic peroxy radical (RO_2) formation, and ring cleavage, leading to ozone and SOA. From combined experimental and theoretical studies, we show that cresol formation is dominant, while primary RO_2 production is negligible. Our work reveals that the formation and subsequent reactions of cresols regulate the atmospheric impacts of toluene oxidation, suggesting that its representation in current atmospheric models should be reassessed for accurate determination of ozone and SOA formation. The results from our study provide important constraints and guidance for future modeling studies.

Author contributions: Y.J. and R.Z. designed research; Y.J., J.Z., H.T., K.M., N.P.L., Y. Li, Y. Lin, J.P., Y.W., L.D., B.P., F.Z., X.F., T.A., W.M.-O., J.S., A.L.Z., K.S., and R.Z. performed research; M.J.M. and R.Z. contributed new reagents/analytic tools; Y.J., M.J.M., and R.Z. analyzed data; and Y.J., J.Z., and R.Z. wrote the paper.

Reviewers: S.M., National Center for Atmospheric Research; and F.Y., State University of New York at Albany.

The authors declare no conflict of interest.

Freely available online through the PNAS open access option.

[1]Y.J. and J.Z. contributed equally to this work.

[2]Present address: Department of Chemistry, Graduate School of Science and Engineering, Tokyo Metropolitan University, Tokyo 192-0364, Japan.

[3]Present address: The Department of Geoscience, University of Wisconsin-Madison, Madison, WI 53706.

[4]To whom correspondence may be addressed. Email: renyi-zhang@tamu.edu, antc99@gdut.edu.cn, or mjmolina@ucsd.edu.

This article contains supporting information online at www.pnas.org/lookup/suppl/doi:10.1073/pnas.1705463114/-/DCSupplemental.

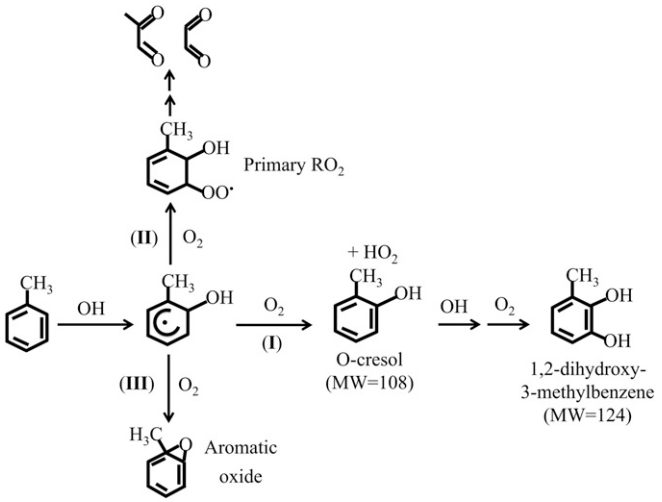

Fig. 1. Competing oxidative pathways of the *ortho* OH–toluene adduct: (pathway I) H abstraction to *o*-cresol, (pathway II) O_2 additiion to form primary *o*-RO_2 and subsequent ring cleavage to form glyoxal and methylglyoxal, and (pathway III) H abstraction followed by O-bridge formation to 1,2-toluene oxide. The chemical mechanism currently adopted in atmospheric models (5) assumes a dominant primary RO_2 production (pathway II) but a minor cresol formation (pathway I).

formation from toluene oxidation is conventionally assumed with a large (65%) contribution from the production of RO_2 (pathway II) and a minor (18%) contribution from HO_2 formed with cresols (pathway I). Both RO_2 and HO_2 generated react with nitric oxide (NO) to yield nitrogen dioxide (NO_2), which subsequently undergoes photodissociation to lead to ozone formation. In addition, aromatic ring cleavage from the primary RO_2 and cresol pathways (pathways I and II) results in several products, including glyoxal, methylglyoxal, and low-volatility compounds that likely contribute to SOA formation (1–3, 8, 28–33).

In this study, we evaluated the detailed oxidation mechanism of the OH–toluene reactions by combining direct experimental measurements and quantum chemical and kinetic rate calculations, to improve the understanding of the pathways leading to ozone and SOA formation in the atmosphere.

Results

Fig. 2*A* depicts a mass spectrum (m/z = 95 to 135) of the OH–toluene reactions in the presence of O_2 and NO under our typical experimental conditions (*SI Appendix*, Fig. S1 and Table S1). The peaks at m/z = 107 and 109 correspond to protonated benzaldehyde ($C_7H_7O^+$) and cresols ($C_7H_9O^+$), respectively. The peak at m/z = 125 is attributed to dihydroxymethylbenzenes ($C_7H_9O_2^+$), corresponding to the secondary products from the subsequent oxidation of cresols initiated by OH (33), to be discussed below. Although the oxide/methyloxepin intermediates correspond to the same molecular weight (MW) as cresols, their formation is excluded because of a large activation barrier for this pathway (16). Fig. 2*B* displays single-ion monitoring of the three products, i.e., benzaldehyde, cresols, and dihydroxymethylbenzenes, versus consumed toluene. The ion–molecule reaction rate constants calculated using the average dipole orientation (ADO) theory (34–36) are 4.1×10^{-9} $cm^3 \cdot molecule^{-1} \cdot s^{-1}$, 2.5×10^{-9} $cm^3 \cdot molecule^{-1} \cdot s^{-1}$, 3.6×10^{-9} $cm^3 \cdot molecule^{-1} \cdot s^{-1}$, and 2.1×10^{-9} $cm^3 \cdot molecule^{-1} \cdot s^{-1}$ for benzaldehyde, cresols (averaged over *o*-, *p*-, and *m*-cresol), dihydroxymethylbenzenes (averaged over 1,2-dihydroxy-3-methylbenzene and 1,2-dihydroxy-4-methylbenzene), and toluene, respectively. The yields of those products are quantified to be (11.3 ± 2.0)% for benzaldehyde, (39.0 ± 5.0)% for cresols, and (8.9 ± 1.3)% for dihydroxymethylbenzenes. Table 1 summarizes our measured product yields, along with comparison with the previous studies.

The yield of 11.3% for benzaldehyde determined in our present work is in agreement with the previous studies reporting a range of 5 to 12% (9, 11, 12, 18). We determined a lower limit of 47.9% for the total branching ratio of the cresol pathway (pathway I), including those from the combined formation of cresols and dihydroxymethylbenzenes. Our estimated cresol yield is much higher than that from most of the previous studies (12, 15, 18, 19, 27). For example, another experimental investigation using a flow reactor in conjunction with chemical ionization mass spectrometry (CIMS) detection reported yields of 28.1% at m/z = 109 and 23.5% at m/z = 125 (18). Although the sum of the two peaks from that work is comparable to our present value, the authors attributed the peak m/z = 125 to dienedial, which was speculated to form from O_2 addition to the OH–toluene adduct followed by breaking of the OH group (18). In addition, it was commented on by Jenkin et al. (37) that the experimental work by Baltaretu et al. (18) might be complicated by possible interferences, because both radicals and the reactants were premixed with high concentrations in the side arm of the flow reactor. Also noticeably, we measured a negligible yield of methylglyoxal (less than 2%), in contrast to the fact that the previous environmental chambers studies consistently observed large amounts of small α-carbonyl compounds (glyoxal and methylglyoxal) as the ring-opening products (12). The negligible formation of methylglyoxal in our current work is also distinct from our previous study of the OH–m-xylene reactions, in which larger amounts of methylglyoxal and the coproducts of glyoxal and methylglyoxal were detected and quantified (35). Baltaretu et al. (18) also reported a small methylgyoxal yield, i.e., less than 4%, consistent with our present work. We did not detect any compound with an MW similar to that of expoxides and estimated the epoxide yield to be less than 1%. Bartolotti and Edney (38) suggested the formation of epoxide intermediates based on the large stability for epoxides, which was further corroborated by Yu and Jeffries (39), who found

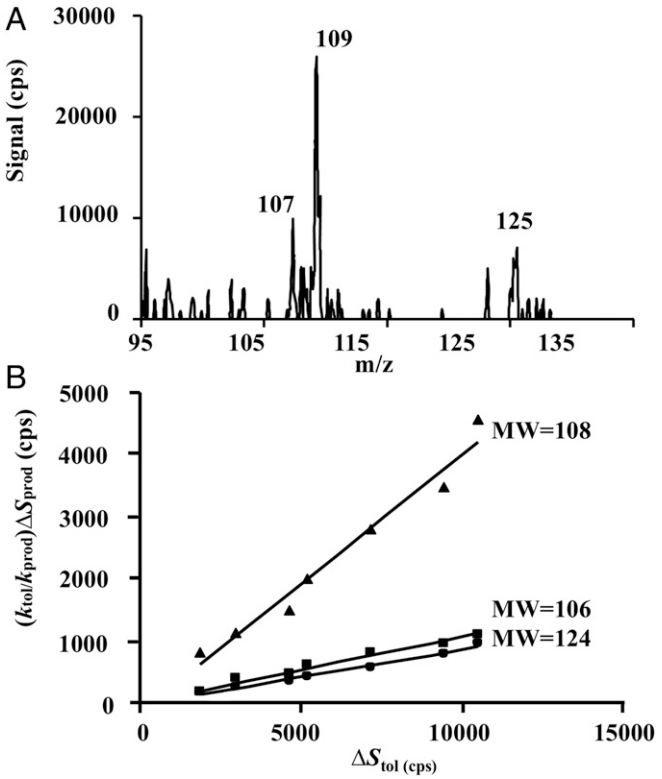

Fig. 2. Detection and quantification of products from OH-initiated oxidation of toluene. (*A*) Mass spectral scan (m/z = 95 to 135) of the OH–toluene reactions under a typical experimental condition. (*B*) Plot of $k_{tol}/k_{prod} \times \Delta S_{prod}$ versus ΔS_{tol}. The slope of the line corresponds to the product yield.

Table 1. Product yields from OH-initiated oxidation of toluene in the presence of O_2 and NO

Product	Product yield	
	Previous work	This work*
Benzaldehyde (MW = 106)	11[†], 5.3[‡], 6.0[§], 4.9[¶], 5.8[#], 6.5[‖]	11.3 ± 2.0
Cresols (MW = 108)	52.9[‡], 15.3[§], 28.1[¶], 17.9[#], 17.2**, 25.2[‖]	39.0 ± 5.0
Dihydroxymethyl-benzenes (MW = 124)		8.9 ± 1.3
MW = 96 (unidentified)		~5
Glyoxal (MW = 58)	9.8[†], 4.1[‡], 23.8[§], 39.0[††]	
Methylglyoxal (MW = 72)	10.6[†], 5.5[‡], 16.7[§], < 4%[¶]	<2
Epoxides (MW = 140)	7.2[¶]	<1

*The yield represents the sum of all isomers, if applicable. Each value represents an average of more than 15 measurements at various experimental conditions (*SI Appendix*, Table S1). The uncertainty reflects both random error due to data scattering and systematic error related to the ion–molecule rate constants and possible fragmentation of the proton transfer reactions. Experimental conditions: [toluene] = (0.2 to 2) × 10^{12} molecules·cm^{-3}, [NO] = (0.5 to 2) × 10^{12} molecules·cm^{-3}, [O_2] = (0.7 to 1.5) × 10^{15} molecules·cm^{-3}, and [OH] = (0.8 to 8) × 10^{10} molecules·cm^{-3}.
[†]From ref. 9.
[‡]From ref. 11.
[§]From ref. 12.
[¶]From ref. 18.
[#]From ref. 19.
[‖]From ref. 27.
**From ref. 15.
[††]From ref. 13.

experimental evidence for epoxides by detecting compounds with MW matching a series of epoxides resulting from the OH–toluene system. However, isomerization of bicyclic radicals to the more stable expoxide radicals has been shown to possess significantly higher barriers than those of O_2 addition to form bicyclic peroxy radicals (16, 26).

To further elucidate the toluene oxidation mechanism and corroborate our experimental results, we performed quantum chemical calculation for OH addition to the *ortho*, *meta*, and *para* positions of toluene and the subsequent reactions with O_2. The potential energy surface diagrams of the toluene reactions are displayed in Fig. 3. OH addition at the *ortho* position occurs with the lowest activation energy (E_a) of 1.2 kcal·mol^{-1} and the largest reaction energy (ΔE_r) of −15.5 kcal·mol^{-1} among the three pathways (Fig. 3*A* and Table 2). The kinetics calculations presented in Table 2 show a rate constant of 2.7×10^{-12} cm^3·molecule^{-1}·s^{-1} for OH *ortho* addition at 298 K, which is an order of magnitude higher than those of OH addition to the *meta* and *para* positions. The branching ratio (Γ) of OH *ortho* addition is estimated to be 76%. The energetics, rate constants, and branching ratios of the OH–toluene reactions are summarized in Table 2, along with comparisons with previously published experimental and theoretical results.

We further evaluated the competing reactions of the OH–toluene adducts with O_2 lead to cresols (pathway I), organic peroxy radicals (RO_2) (pathway II), and toluene oxide (pathway III). *SI Appendix*, Fig. S2 shows that the reaction of the *ortho* OH adduct with O_2 to form 1,2-toluene oxide occurs with an E_a value of 33.6 kcal·mol^{-1} and a ΔE_r value of 16.2 kcal·mol^{-1}. Hence, the large activation energy and instability of the toluene oxide imply that its formation is thermodynamically and kinetically inhibited, in agreement with the previous studies (26). Our previous theoretical study indicated that, at each OH addition site, only one isomeric pathway via the peroxy radical is accessible for ring cleavage (16). On the basis of that study (16), the preferred peroxy radical corresponds to O_2 additions at the C_3 position (*o*-RO_2 and *p*-RO_2) for the *ortho* and *para* OH–toluene adducts, respectively, and at the C_6 position (*m*-RO_2) for the *meta* OH–toluene adduct. As illustrated in Fig. 3*A* and Table 2, the E_a value to form *o*-cresol is 4.4 kcal·mol^{-1}, which is lower by 3.1 kcal·mol^{-1} than that to form *o*-RO_2, and *o*-cresol is by 17.8 kcal·mol^{-1} more stable than *o*-RO_2. The rate constant calculated is 1.6×10^{-15} cm^3·molecule^{-1}·s^{-1} for *o*-cresol formation (Table 2). In contrast, the E_a values to form *p*- and *m*-cresol are larger than those to form *p*- and *m*-RO_2, although both *p*- and *m*-cresols are more stable (by about 15 kcal·mol^{-1}) than *p*- and *m*-RO_2, and the Γ values calculated are 9% and 3%, respectively, to form *p*- and *m*-cresol. The fate of the primary RO_2 is governed by the competition between decomposition back to the OH–toluene adducts and O_2 cyclization to form bridged bicyclic radicals. *SI Appendix*, Fig. S3 shows that the E_a values for RO_2 decomposition are smaller than those of cyclization for *p*- and *m*-RO_2. Considering the large differences in the relative stability between cresols and primary RO_2 and the high E_a values for *p*- and *m*-RO_2 cyclization, the majority of RO_2 formed from the two channels shifts reversibly to cresols by equilibrium. Hence, we conclude that cresol formation represents the nearly exclusive pathway for the OH-addition reactions.

We performed additional calculations of the subsequent reactions of *o*-cresol with OH and O_2 (Fig. 3*B*). OH addition at C_3 position of *o*-cresol occurs with an E_a value of −0.4 kcal·mol^{-1} and a ΔE_r value of −15.6 kcal·mol^{-1}, corresponding to a rate coefficient of 4.3×10^{-11} cm^3·molecule^{-1}·s^{-1} to form the dihydroxymethybenzyl (DHMB) radical. Subsequently, the C_3 DHMB radical undergoes readily H abstraction by O_2, with an E_a value of 2.2 kcal·mol^{-1} and a ΔE_r value of −26.5 kcal·mol^{-1}, corresponding to a rate coefficient of 5.4×10^{-12} cm^3·molecule^{-1}·s^{-1} to form 1,2-dihydroxy-3-methylbenzene (MW = 124). In contrast, the formation of aromatic ketones (also MW = 124) is both thermodynamically and kinetically hindered (*SI Appendix*, Fig. S4). Hence, our theoretical calculations support the formation of dihydroxymethylbenzenes as the observed mass peak at m/z = 125. Our theoretical predictions agree with two previous experimental results, showing that the major oxidation products from the reactions of cresols with OH are dihydroxymethylbenzenes with a molar yield of 65 to 73% (33, 40). Furthermore, a fast rate constant of (1.6 to 2.1) × 10^{-10} cm^3·molecule^{-1}·s^{-1} for the reaction of dihydroxymethylbenzenes with OH has been reported (40, 41),

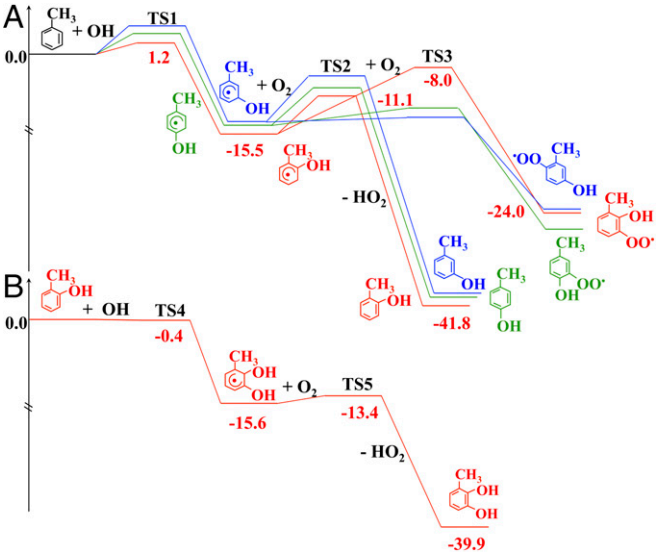

Fig. 3. Potential energy surfaces of the OH–toluene reaction. (*A*) Addition to the *ortho*, *meta*, and *para* positions and the subsequent reactions with O_2. (*B*) Addition of OH to *o*-cresol and the subsequent reaction with O_2. The number denotes the energetics in kcal·mol^{-1}.

Table 2. Summary of activation energy (E_a, kcal·mol^{-1}), reaction energy (ΔE_r, kcal·mol^{-1}), rate constant (k, cm^3·molecule^{-1}·s^{-1}), and branching ratio (Γ) of the OH–toluene reactions at 298 K

Reactions	Quantity	*Ortho*	*Para*	*Meta*
Toluene + OH → OH adduct	E_a	1.2	2.1	2.7
	ΔE_r	−15.5	−14.6	−14.4
	k	2.7×10^{-12}	7.4×10^{-13}	1.2×10^{-13}
	Γ, %	74*, 80.6†, 52‡, 59	21*, 14.3†, 34‡, 14	3*, 5.1†, 11‡, 5
OH-adduct + O_2 → cresol	E_a	4.4§, 3.7	4.1	5.0
	ΔE_r	−26.3§, −28.7	−26.8	−27.0
	k	1.6×10^{-15}‡, 0.9×10^{-15}§, 5.1×10^{-15}	2.4×10^{-15}‡, 1.7×10^{-15}	1.2×10^{-16}
OH-adduct + O_2 → RO_2	E_a	7.5§, 7.1	0.8	−0.4
	ΔE_r	−8.5§,−2.9	−12.2	−9.5
	k	1.5×10^{-16}‡, 2.8×10^{-16}§, 1.0×10^{-17}¶, 3×10^{-15}	2.5×10^{-14}‡, 1.5×10^{-14}	4.5×10^{-15}
O-cresol + OH → DHMB	E_a	−0.4		
	ΔE_r	−15.6		
	k	4.3×10^{-11}#, 4.3×10^{-11}		
DHMB + O_2 → 1,2-dihydroxy-3-ethylbenzene	E_a	2.2		
	ΔE_r	−24.3		
	k	5.4×10^{-12}		

The value is from the present work, except noted otherwise. Γ is calculated by excluding those from the OH *ipso* addition and the H-abstraction pathways.
*From ref. 30.
†From ref. 22, including a branching ratio of 3% for OH *ipso* addition.
‡From ref. 23, including a branching ratio of 15% for *ipso* position.
§From ref. 26.
¶From ref. 10.
#From ref. 41.

indicating that the secondary products in the OH–toluene reactions undergo additional reactions with OH to form ring-opening products, including small α-carbonyl compounds (glyoxal and methylglyoxal), organic acids, and other low-volatility products (33).

As is evident from Table 2, our calculations of the energetics, rate constants, and branching ratios for the OH–toluene reactions compare favorably with the previously available experimental and theoretical results, considering the respective uncertainties. For example, our calculated rate coefficient of 4.3×10^{-11} cm^3·molecule^{-1}·s^{-1} for OH addition to *o*-cresol to form the DHMB radical is in agreement with the experimental value of $(4.3 \pm 0.5) \times 10^{-11}$ cm^3·molecule^{-1}·s^{-1} by Coeur-Tourneur et al. (41). Additional structural parameters for the reactants, key intermediates, transition states, and products involved in the OH–toluene reaction system are shown in *SI Appendix*, Fig. S5.

Hence, our combined experimental and theoretical methods (42–60) provide kinetic and mechanistic insights into the OH–toluene reactions. In particular, the agreement between our experimental and theoretical results provides compelling evidence for the dominant cresol yield but a negligible formation of methylglyoxal from the initial steps of the OH–toluene reactions. In our work, we quantified only the most abundant peaks detected by our ion drift (ID)-CIMS scheme (using H_3O^+), accounting for about 64% of the toluene consumed. Another recent experimental study showed that OH addition to the aromatic ring of *o*-cresol leads to hydroxy, dihydroxy, and trihydroxy methyl benzoquinones and dihydroxy, trihydroxy, tetrahydroxy, and pentahydroxy toluenes, detected in the gas phase by CIMS (using CF_3O^- and $H^+ \cdot nH_2O$ where $n = 1, 2, \ldots$) and in the particle phase using offline direct analysis with real-time mass spectrometry (33).

The differences in the measured product yields between our present experimental work and the previous laboratory experiments are explainable by the distinct conditions among the various experimental studies. Although the environmental chamber method has been applied extensively in development of parameterizations of formation of ozone and SOA for atmospheric modeling purposes (5), there were several intricate difficulties for the chamber approach, which made it rather unsuitable for detailed kinetic and mechanistic investigations of atmospheric hydrocarbon chemistry. Specifically, the limitations in the earlier chamber studies included longer reaction times (minutes to hours), higher reactant concentrations, wall loss, and the lack of online detection and quantification of reactive reactants and products by advanced analytical instruments. For example, an earlier experimental study reported a yield of 25.2% for the cresols from the OH–toluene reactions (27). The concentrations of the reactants used in that study were about 4×10^{13} and 1×10^{13} molecules·cm^{-3} for toluene and NO_x, respectively, and the OH concentration was not measured but was estimated from the decay in the toluene concentration. The concentrations of the reactants and products were measured by using offline gas chromatography with flame ionization detection. For the irradiation time of about 10 min during their chamber experiments, a lifetime of cresols was estimated to be about 230 s, using the rate coefficient of 4.3×10^{-11} cm^3·molecule^{-1}·s^{-1} for the reaction between cresols and OH from this work and another experimental study (40). Hence, there likely existed significant secondary reactions of cresols with OH in the earlier chamber investigations, responsible for the measured lower cresol yields in the majority of those studies (12, 19, 27).

On the other hand, the technique of high-pressure turbulent flow reactors in conjunction with CIMS detection has been developed for accurate kinetic measurements of atmospheric gas-phase reactions (35, 36). The main advantage of the fast-flow reactor system lies in the ability to isolate the individual reaction steps and intermediates (35, 36, 42–44, 48, 61). Specifically, the CIMS technique allows for online detection of many reactants, intermediates, and products with high sensitivity and selectivity (35, 36). In addition, the ID-CIMS method provides quantification of the gas-phase concentrations of the intermediates and products without the necessity of calibration, which is advantageous because of the general difficulty in obtaining the authentic standards for products of hydrocarbon reactions (34–36). Furthermore, a turbulent flow condition effectively minimizes the wall loss (35, 36). In our experiments, the reactant concentrations were $(0.4 \text{ to } 1.6) \times 10^{12}$ and $(5.4 \text{ to } 19) \times 10^{12}$ molecules·cm^{-3} for toluene and NO_2, respectively, about one to two orders of magnitude lower than those of the environmental chamber studies (12, 19, 27). In addition, the OH concentration was directly quantified in our experiments, in a range of $(0.8 \text{ to } 8.0) \times 10^{10}$ molecules·cm^{-3}. Secondary reactions were

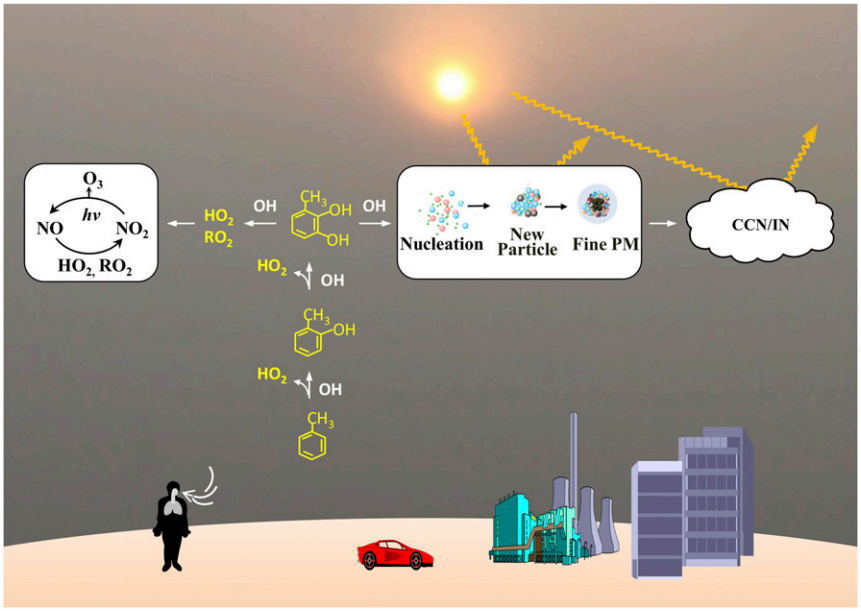

Fig. 4. Toluene oxidation and urban photochemical smog. The OH–toluene reactions lead promptly and dominantly to cresol formation, which regulates the impacts on air quality, human health, and climate. The phenolic pathway yields HO_2 and RO_2 that facilitate ozone production by converting NO to NO_2, as photodissociation of NO_2 occurs in the wavelength range of 400 nm to 650 nm (the symbol *hv* denotes the energy of a photon, where *h* is the Planck number and *v* is the frequency of light). Also, dihydroxymethylbenzenes generated from this pathway undergo subsequent reactions with OH to form the precursors for aerosol nucleation and growth, including small α-carbonyl compounds, organic acids, and other highly oxygenated low-volatility products.

effectively suppressed in our experiments because of the short reaction time in the flow reactor (on the order of about 50 ms). The lifetime of cresols was estimated to be about 2 s in our experiments, responsible for our measured high yield of cresols. Under our experimental conditions, the self-reaction of the OH–toluene adducts was unimportant on the basis of this rate constant reported previously (10); this reaction was estimated to be about one to two orders of magnitude lower than that of the OH–toluene adduct with O_2. Furthermore, the absolute O_2 concentration had no effect for the competing reactions between the cresol and primary RO_2 pathways (i.e., pathway I vs. pathway II in Fig. 1), and the previous experimental results did not show a pressure dependence of the OH–toluene reaction system (61).

Also, our theoretical calculations indicate that formation of glyoxal and methylglyoxal via primary RO_2 is minimal, consistent with the absence in the ring-opening α-carbonyl products detected in our experiments. It is anticipated that those species are formed as the multigeneration products from the cresol pathway (33), likely similar to the cases with their high yields in the previous chamber experiments (12, 13).

Conclusion

Photochemical oxidation of toluene contributes importantly to ozone and SOA formation in urban environments, with key implications for air quality and human health (1–3, 62). In addition, by directly scattering and absorbing solar radiation and indirectly serving as cloud condensation nuclei or ice nuclei, SOA represents the major component in global radiative forcing on climate (1–3). For toluene oxidation, ozone formation in current atmospheric models is represented mainly via primary RO_2, with a minor contribution from cresols (5). In contrast, our experimental and theoretical results reveal the exclusive prompt productions of cresols and HO_2, but insignificant formation of primary RO_2 from the reaction of OH–toluene adducts with O_2. HO_2 is also produced from the reaction of cresols with OH, and further reactions of dihydroxymethylbenzenes with OH yield additional HO_2 and RO_2. As a result, the production of HO_2 and RO_2 along the phenolic pathway regulates the abundance of the total peroxy radicals, which facilitates the conversion between NO and NO_2 (Fig. 4). In addition, the relative branching between the RO_2 and cresol pathways likely affects the OH radical propagation and termination, which are also important for ozone formation.

The further oxidation of dihydroxymethylbenzenes by OH leads to formation of small α-dicarbonyl compounds (glyoxal and methylglyoxal), organic acids, and other low-volatility products (33, 40), which likely contribute to aerosol nucleation and growth by partitioning and particle-phase reactions (1, 63–65). In particular, the recent experimental study by Schwantes et al. (33) has identified a substantial fraction of highly oxygenated low-volatility products, contributing to 20 to 40% of SOA formation from the cresol oxidation initiated by OH radicals.

Our combined experimental and theoretical results show that the prompt formation of cresols and their subsequent oxidation largely regulate the atmospheric impacts of toluene oxidation (Fig. 4), indicating that the representation of the toluene oxidation mechanism should be reassessed in current atmospheric models. Future studies are necessary to incorporate the kinetic and mechanistic results from our present work into atmospheric models, to accurately assess ozone and SOA formation under polluted environments.

Materials and Methods

The experiments were performed using a fast-flow reactor in conjunction with ID-CIMS. Detailed description of the ID-CIMS technique can be found in our previous publications (42–44).

Quantum chemical calculations were performed with the Gaussian 09 suite of programs (45). Geometry optimization of the relevant species were executed at the M06-2X level with the standard 6-311G(d,p) basis set [M06-2X/6-311G(d,p)]. This level of theory has been successfully applied to atmospheric reactions (46, 47). The vibrational analysis was made at the same level of theory to characterize the nature of each critical point along the potential energy surface (PES) with a local minimum or a transition state (exactly one imaginary frequency) and to make zero-point-energy corrections. The minimum-energy path was constructed with the intrinsic reaction coordinate theory to confirm that the transition state connected with the minima along the reaction path. Because kinetic calculations of the organic reaction systems were highly sensitive to the predicted energetics (48–51), single-point energy calculations were performed to refine the PES using the QCISD(T)/6-311+G(2d,p) level. The dual-level potential profile along the reaction path was further refined with the interpolated single-point energy method (52), in which extra single-point calculations were performed to correct the lower-level reaction path. The dual-level dynamics approach was denoted as X//Y, where a single-point energy calculation at level X was carried out for the geometry optimized at a lower level Y. Using the Polyrate 2010A (53) and KiSThelp programs (54), the rate constants were calculated according to the canonical variational transition state theory (55–59), along with the small curvature tunneling correction (60).

Additional descriptions of the experimental conditions and the structure of the reactants, products, intermediates, and transition states are provided in *SI Appendix*.

ACKNOWLEDGMENTS. This work was supported by National Natural Science Foundation of China (Grants 41675122, 41373102, 21577177, and 41425015), Science and Technology Program of Guangzhou City (Grant 201707010188), the Robert A. Welch Foundation (Grant A-1417), the Ministry of Science and Technology of China (Grant 2013CB955800), and a collaborative research program between Texas A&M University and the National Natural Science Foundation of China. B.P. was supported by a NASA Earth and Space Science Fellowship Program, and W.M.-O. was supported by the National Science Foundation Graduate Research Fellowship Program. Additional support for this research was provided by the Texas A&M University Supercomputing Facilities. The authors acknowledge the use of the Laboratory for Molecular Simulations at Texas A&M.

1. Zhang R, et al. (2015) Formation of urban fine particulate matter. *Chem Rev* 115: 3803–3855.
2. Seinfeld JH, Pandis SN (2006) *Atmospheric Chemistry and Physics: From Air Pollution to Climate Change* (John Wiley, Hoboken, NJ).
3. Finlayson–Pitts BJ, Pitts JN, Jr (1999) *Chemistry of the Upper and Lower Atmosphere: Theory, Experiments, and Applications* (Academic, San Diego).
4. Calvert JG, et al. (2002) *The Mechanisms of Atmospheric Oxidation of the Aromatic Hydrocarbons* (Oxford Univ Press, Oxford).
5. Whitten GZ, et al. (2010) A new condensed toluene mechanism for carbon bond: CB05-TU. *Atmos Environ* 44:5346–5355.
6. Guo S, et al. (2014) Elucidating severe urban haze formation in China. *Proc Natl Acad Sci USA* 111:17373–17378.
7. Ng NL, et al. (2007) Secondary organic aerosol formation from m-xylene, toluene, and benzene. *Atmos Chem Phys* 7:3909–3922.
8. Lee-Taylor J, et al. (2011) Explicit modeling of organic chemistry and secondary organic aerosol partitioning for Mexico City and its outflow plume. *Atmos Chem Phys* 11:13219–13241.
9. Gery MW, et al. (1985) A continuous stirred tank reactor investigation of the gas-phase reaction of hydroxyl radicals and toluene. *Int J Chem Kinet* 17:931–955.
10. Bohn B (2001) Formation of peroxy radicals from OH–toluene adducts and O_2. *J Phys Chem A* 105:6092–6101.
11. Seuwen R, Warneck P (1996) Oxidation of toluene in NO_x free air: Product distribution and mechanism. *Int J Chem Kinet* 28:315–332.
12. Smith D, McIver C, Kleindienst T (1998) Primary product distribution from the reaction of hydroxyl radicals with toluene at ppb NOx mixing ratios. *J Atmos Chem* 30: 209–228.
13. Volkamer R, Platt U, Wirtz K (2001) Primary and secondary glyoxal formation from aromatics: Experimental evidence for the bicycloalkyl-radical pathway from benzene, toluene, and p-xylene. *J Phys Chem A* 105:7865–7874.
14. Uc VH, Alvarez-Idaboy JR, Galano A, García-Cruz I, Vivier-Bunge A (2006) Theoretical determination of the rate constant for OH hydrogen abstraction from toluene. *J Phys Chem A* 110:10155–10162.
15. Noda J, Volkamer R, Molina MJ (2009) Dealkylation of alkylbenzenes: A significant pathway in the toluene, *o*-, *m*-, *p*-xylene + OH reaction. *J Phys Chem A* 113: 9658–9666.
16. Suh I, Zhang R, Molina LT, Molina MJ (2003) Oxidation mechanism of aromatic peroxy and bicyclic radicals from OH–toluene reactions. *J Am Chem Soc* 125:12655–12665.
17. Birdsall AW, Elrod MJ (2011) Comprehensive NO-dependent study of the products of the oxidation of atmospherically relevant aromatic compounds. *J Phys Chem A* 115: 5397–5407.
18. Baltaretu CO, Lichtman EI, Hadler AB, Elrod MJ (2009) Primary atmospheric oxidation mechanism for toluene. *J Phys Chem A* 113:221–230.
19. Klotz B, et al. (1998) Atmospheric oxidation of toluene in a large-volume outdoor photoreactor: In situ determination of ring-retaining product yields. *J Phys Chem A* 102:10289–10299.
20. Gómez Alvarez E, Viidanoja J, Muñoz A, Wirtz K, Hjorth J (2007) Experimental confirmation of the dicarbonyl route in the photo-oxidation of toluene and benzene. *Environ Sci Technol* 41:8362–8369.
21. Birdsall AW, Andreoni JF, Elrod MJ (2010) Investigation of the role of bicyclic peroxy radicals in the oxidation mechanism of toluene. *J Phys Chem A* 114:10655–10663.
22. Suh I, Zhang D, Zhang R, Molina LT, Molina MJ (2002) Theoretical study of OH addition reaction to toluene. *Chem Phys Lett* 364:454–462.
23. Wu R, Pan S, Li Y, Wang L (2014) Atmospheric oxidation mechanism of toluene. *J Phys Chem A* 118:4533–4547.
24. Suh I, Zhao J, Zhang R (2006) Unimolecular decomposition of aromatic bicyclic alkoxy radicals and their acyclic radicals. *Chem Phys Lett* 432:313–320.
25. Frankcombe TJ (2008) OH-initiated oxidation of toluene. 3. Low-energy routes to cresol and oxoheptadienal. *J Phys Chem A* 112:1572–1575.
26. Huang MQ, et al. (2008) Theoretical investigation on the mechanism and kinetics of toluene-OH adduct with oxygen molecule. *J Mol Struc Theochem* 862:28–32.
27. Akintson R, Aschmann SM, Arey J, Carter WPL (1989) Formation of ring-retaining products from the OH radical-initiated reactions of benzene and toluene. *Int J Chem Kinet* 21:801–827.
28. Zhang R, et al. (2004) Atmospheric new particle formation enhanced by organic acids. *Science* 304:1487–1490.
29. Gomez ME, Lin Y, Guo S, Zhang R (2015) Heterogeneous chemistry of glyoxal on acidic solutions. An oligomerization pathway for secondary organic aerosol formation. *J Phys Chem A* 119:4457–4463.
30. Zhao J, Levitt NP, Zhang R, Chen J (2006) Heterogeneous reactions of methylglyoxal in acidic media: Implications for secondary organic aerosol formation. *Environ Sci Technol* 40:7682–7687.
31. Kenley RA, Davenport JE, Hendry DG (1981) Gas-phase hydroxyl radical reactions. Products and pathways for the reaction of hydroxyl with aromatic hydrocarbons. *J Phys Chem* 85:2740–2746.
32. Qiu C, Khalizov AF, Zhang R (2012) Soot aging from OH-initiated oxidation of toluene. *Environ Sci Technol* 46:9464–9472.
33. Schwantes RH, et al. (2017) Formation of highly oxygenated low-volatility products from cresol oxidation. *Atmos Chem Phys* 17:3453–3474.
34. Zhao J, Zhang R (2004) Proton transfer reaction rate constants between hydronium ion (H_3O^+) and volatile organic compounds (VOCs). *Atmos Environ* 38:2177–2185.
35. Zhao J, Zhang R, Misawa K, Shibuya K (2005) Experimental product study of the OH-initiated oxidation of *m*-xylene. *J Photoch Photobio A* 176:199–207.
36. Zhao J, Zhang R, Fortner EC, North SW (2004) Quantification of hydroxycarbonyls from OH–isoprene reactions. *J Am Chem Soc* 126:2686–2687.
37. Jenkin ME, Glowacki DR, Rickard AR, Pilling MJ (2009) Comment on "Primary atmospheric oxidation mechanism for toluene." *J Phys Chem A* 113:8136–8138, discussion 8139–8140.
38. Bartolotti LJ, Edney EO (1995) Density functional theory derived intermediates from the OH initiated atmospheric oxidation of toluene. *Chem Phys Lett* 245:119–122.
39. Yu J, Jeffries HE (1997) Atmospheric photooxidation of alkylbenzenes—II. Evidence of formation of epoxide intermediates. *Atmos Environ* 31:2281–2287.
40. Olariu RI, Klotz B, Barnes I, Becker KH, Mocanu R (2002) FT–IR study of the ring-retaining products from the reaction of OH radicals with phenol, *o*-, *m*-, and *p*-cresol. *Atmos Environ* 36:3685–3697.
41. Coeur-Tourneur C, Henry F, Janquin MA, Brutier L (2006) Gas-phase reaction of hydroxyl radicals with *m*-, *o*- and *p*-cresol. *Int J Chem Kinet* 38:553–562.
42. Zhang R, Suh I, Lei W, Clinkenbeard AD, North SW (2000) Kinetic studies of OH-initiated reactions of isoprene. *J Geophys Res* 105:24627–24635.
43. Fortner EC, Zhao J, Zhang R (2004) Development of ion drift-chemical ionization mass spectrometry. *Anal Chem* 76:5436–5440.
44. Zhang D, Zhang R, North SW (2003) Experimental study of NO reaction with isoprene hydroxyalkyl peroxy radicals. *J Phys Chem A* 107:11013–11019.
45. Frisch MJ, et al. (2009) *Gaussian 09, Revision A.02* (Gaussian, Wallingford, CT).
46. Ellingson BA, Truhlar DG (2007) Explanation of the unusual temperature dependence of the atmospherically important OH + $H_2S \rightarrow H_2O$ + HS reaction and prediction of the rate constant at combustion temperatures. *J Am Chem Soc* 129:12765–12771.
47. Pan S, Wang L (2014) Atmospheric oxidation mechanism of *m*-xylene initiated by OH radical. *J Phys Chem A* 118:10778–10787.
48. Suh I, Lei W, Zhang R (2001) Experimental and theoretical studies of isoprene reaction with NO_3. *J Phys Chem A* 105:6471–6478.
49. Zhang D, Zhang R (2002) Mechanism of OH formation from ozonolysis of isoprene: A quantum-chemical study. *J Am Chem Soc* 124:2692–2703.
50. Zhang D, Lei W, Zhang R (2002) Mechanism of OH formation from ozonolysis of isoprene: Kinetics and product yields. *Chem Phys Lett* 358:171–179.
51. Lei W, Zhang R (2001) Theoretical study of hydroxy-isoprene alkoxy radicals and their decomposition pathways. *J Phys Chem A* 105:3808–3815.
52. Chuang YY, Corchado JC, Truhlar DG (1999) Mapped interpolation scheme for single-point energy corrections in reaction rate calculations and a critical evaluation of dual-level reaction path dynamics methods. *J Phys Chem A* 103:1140–1149.
53. Zheng J, et al. (2010) *Polyrate 2010-A* (Univ Minnesota, Minneapolis, MN).
54. Canneaux S, Bohr F, Henon E (2014) KiSThelP: A program to predict thermodynamic properties and rate constants from quantum chemistry results. *J Comput Chem* 35: 82–93.
55. Gonzalez-Lafont A, Truong TN, Truhlar DG (1991) Direct dynamics calculations with neglect of diatomic differential overlap molecular orbital theory with specific reaction parameters. *J Phys Chem* 95:4618–4627.
56. Lei W, Zhang Z, McGivern WS, Derecskei-Kovacs A, North SW (2001) Theoretical study of OH-O_2-isoprene peroxy radicals. *J Phys Chem A* 105:471–477.
57. Lei W, Derecskei-Kovacs A, Zhang R (2000) Ab initio study of OH addition reaction to isoprene. *J Phys Chem A* 113:5354–5360.
58. Zhang D, Zhang R, Park J, North SW (2002) Hydroxy peroxy nitrites and nitrates from OH initiated reactions of isoprene. *J Am Chem Soc* 124:9600–9605.
59. Lei W, Zhang Z, McGivern WS, Derecskei-Kovacs A, North SW (2000) Theoretical study of isomeric branching in the isoprene-OH reaction: Implications to final product yields in isoprene oxidation. *Chem Phys Lett* 326:109–114.
60. Liu YP, Lu DH, Gonzalez-Lafont A, Truhlar DG, Garrett BC (1993) Direct dynamics calculation of the kinetic isotope effect for an organic hydrogen-transfer reaction, including corner-cutting tunneling in 21 dimensions. *J Am Chem Soc* 115:7806–7817.
61. Molina MJ, et al. (1999) Experimental study of intermediates from OH-initiated reactions of toluene. *J Am Chem Soc* 121:10225–10226.
62. Zhang R, Lei W, Tie X, Hess P (2004) Industrial emissions cause extreme urban ozone diurnal variability. *Proc Natl Acad Sci USA* 101:6346–6350.
63. Zhao J, Khalizov A, Zhang R, McGraw R (2009) Hydrogen-bonding interaction in molecular complexes and clusters of aerosol nucleation precursors. *J Phys Chem A* 113:680–689.
64. Xu Y, Nadykto AB, Yu F, Herb J, Wang W (2010) Interaction between common organic acids and trace nucleation species in the Earth's atmosphere. *J Phys Chem A* 114: 387–396.
65. Peng J, et al. (2016) Markedly enhanced absorption and direct radiative forcing of black carbon under polluted urban environments. *Proc Natl Acad Sci USA* 113: 4266–4271.